Cross sections for ν_μ and $\bar{\nu}_\mu$ induced pion production on hydrocarbon in the few-GeV region using MINERvA

C.L. McGivern,[1,*] T. Le,[2,3] B. Eberly,[1,†] L. Aliaga,[4,5] O. Altinok,[2] L. Bellantoni,[6] A. Bercellie,[7] M. Betancourt,[6] A. Bodek,[7] A. Bravar,[8] H. Budd,[7] T. Cai,[7] M.F. Carneiro,[9] M.E. Christy,[10] H. da Motta,[9] S.A. Dytman,[1] G.A. Díaz,[7,5] E. Endress,[5] J. Felix,[11] L. Fields,[6,12] R. Fine,[7] R.Galindo,[13] H. Gallagher,[2] T. Golan,[7,6] R. Gran,[14] D.A. Harris,[6] A. Higuera,[7,11,‡] K. Hurtado,[9,15] M. Kiveni,[6] J. Kleykamp,[7] M. Kordosky,[4] E. Maher,[16] S. Manly,[7] W.A. Mann,[2] C.M. Marshall,[7] D.A. Martinez Caicedo,[9,§] K.S. McFarland,[7,6] A.M. McGowan,[7] B. Messerly,[1] J. Miller,[13] A. Mislivec,[7] J.G. Morfín,[6] J. Mousseau,[17,¶] D. Naples,[1] J.K. Nelson,[4] A. Norrick,[4] Nuruzzaman,[3,13] V. Paolone,[1] J. Park,[7] C.E. Patrick,[12] G.N. Perdue,[6,7] L. Rakotondravohitra,[6,**] M.A. Ramirez,[11] R.D. Ransome,[3] H. Ray,[17] L. Ren,[1] D. Rimal,[17] P.A. Rodrigues,[7] D. Ruterbories,[7] H. Schellman,[18,12] D.W. Schmitz,[19,6] C. Simon,[20] C.J. Solano Salinas,[15] S. Sánchez Falero,[5] B.G. Tice,[3] E. Valencia,[11] T. Walton,[10,††] J. Wolcott,[7,‡‡] M.Wospakrik,[17] and D. Zhang[4]

[1] *Department of Physics and Astronomy, University of Pittsburgh, Pittsburgh, Pennsylvania 15260, USA*
[2] *Physics Department, Tufts University, Medford, Massachusetts 02155, USA*
[3] *Rutgers, The State University of New Jersey, Piscataway, New Jersey 08854, USA*
[4] *Department of Physics, College of William & Mary, Williamsburg, Virginia 23187, USA*
[5] *Sección Física, Departamento de Ciencias, Pontificia Universidad Católica del Perú, Apartado 1761, Lima, Perú*
[6] *Fermi National Accelerator Laboratory, Batavia, Illinois 60510, USA*
[7] *University of Rochester, Rochester, New York 14627 USA*
[8] *University of Geneva, 1211 Geneva 4, Switzerland*
[9] *Centro Brasileiro de Pesquisas Físicas, Rua Dr. Xavier Sigaud 150, Urca, Rio de Janeiro, Rio de Janeiro, 22290-180, Brazil*
[10] *Hampton University, Dept. of Physics, Hampton, VA 23668, USA*
[11] *Campus León y Campus Guanajuato, Universidad de Guanajuato, Lascurain de Retana No. 5, Colonia Centro, Guanajuato 36000, Guanajuato México.*
[12] *Northwestern University, Evanston, Illinois 60208*
[13] *Departamento de Física, Universidad Técnica Federico Santa María, Avenida España 1680 Casilla 110-V, Valparaíso, Chile*
[14] *Department of Physics, University of Minnesota – Duluth, Duluth, Minnesota 55812, USA*
[15] *Universidad Nacional de Ingeniería, Apartado 31139, Lima, Perú*
[16] *Massachusetts College of Liberal Arts, 375 Church Street, North Adams, MA 01247*
[17] *University of Florida, Department of Physics, Gainesville, FL 32611*
[18] *Department of Physics, Oregon State University, Corvallis, Oregon 97331, USA*
[19] *Enrico Fermi Institute, University of Chicago, Chicago, IL 60637 USA*
[20] *Department of Physics and Astronomy, University of California, Irvine, Irvine, California 92697-4575, USA*

(Dated: August 22, 2016)

Separate samples of charged-current pion production events representing two semi-inclusive channels ν_μ-CC(π^+) and $\bar{\nu}_\mu$-CC(π^0) have been obtained using neutrino and antineutrino exposures of the MINERvA detector. Distributions in kinematic variables based upon $\mu^\pm$-track reconstructions are analyzed and compared for the two samples. The differential cross sections for muon production angle, muon momentum, and four-momentum transfer Q^2, are reported, and cross sections versus neutrino energy are obtained. Comparisons with predictions of current neutrino event generators are used to clarify the role of the $\Delta(1232)$ and higher-mass baryon resonances in CC pion production and to show the importance of pion final-state interactions. For the ν_μ-CC(π^+) ($\bar{\nu}_\mu$-CC(π^0)) sample, the absolute data rate is observed to lie below (above) the predictions of some of the event generators by amounts that are typically 1-to-2 σ. However the generators are able to reproduce the shapes of the differential cross sections for all kinematic variables of either data set.

PACS numbers: 13.15.+g, 14.20.Gk, 14.60.Lm

arXiv:1606.07127v4 [hep-ex] 19 Aug 2016

* now at Fermi National Accelerator Laboratory, Batavia, IL 60510, USA
† now at SLAC National Accelerator Laboratory, Stanford, CA 94309, USA
‡ now at University of Houston, Houston, TX 77204, USA
§ now at Illinois Institute of Technology, Chicago, IL 60616, USA
¶ now at University of Michigan, Ann Arbor, MI 48109, USA
** also at Department of Physics, University of Antananarivo, Madagascar
†† now at Fermi National Accelerator Laboratory, Batavia, IL 60510, USA
‡‡ now at Tufts University, Medford, MA 02155, USA

I. INTRODUCTION

Interactions of few-GeV neutrinos and antineutrinos with nuclei are of keen interest to present and future neutrino oscillation experiments, such as T2K, NOvA, DUNE, and HyperKamiokande [1–4]. In this energy region, charged-current single-pion production (CC(π)) competes with quasielastic scattering in terms of the total charged-current (CC) event rate observed in the near and far detectors of the neutrino oscillation experiments. In $\nu_\mu/\bar{\nu}_\mu$ CC scattering on nuclei, the nuclear medium enables directly-produced CC(π) states to morph into other final-state pion channels and into quasielastic-like scattering topologies as well. These cross-channel migrations involve energy transfer from the produced state to the struck nucleus, rendering the total final-state energy difficult to detect. In this way distortions are introduced into the reconstruction of neutrino energy E_ν, four-momentum transfer squared Q^2, and hadronic invariant mass W. Obtaining precise knowledge of the observed CC(π) rates and relating them to the various ways that directly-produced states can feed into the final states actually observed, is crucial for continued progress in neutrino oscillation measurements.

Two previous publications [5, 6] reported the MINERvA experiment's first measurements of CC pion production on hydrocarbon (CH) in the channels

$$\nu_\mu + \mathrm{CH} \rightarrow \mu^- + n\pi^\pm + X, \tag{1}$$

$$\bar{\nu}_\mu + \mathrm{CH} \rightarrow \mu^+ + \pi^0 + X'. \tag{2}$$

For both of these CC reactions it is possible to reconstruct the incident neutrino energy, E_ν, the squared four-momentum transfer to the struck nucleus, Q^2, and the invariant hadronic mass, W. Through event selection, the charged pion sample of process (1) is dominated by π^+ production. The data in Ref. [5] was presented in two different ways - a single-pion sample with $W < 1.4\,\mathrm{GeV}$ and an n-pion sample with $W < 1.8\,\mathrm{GeV}$ where n signifies one or more charged pions. The sample selection for the latter sample (same as the data presented here) is for a semi-inclusive process; X may include, in addition to the recoil nucleon, neutral pions, and other particles (nucleons and photons) released by nuclear de-excitation and final-state interactions (FSI). The neutral pion sample of reaction (2) is more nearly exclusive [6]. The sample is restricted to events having one and only one π^0, with no visible charged tracks other than the μ^+ emerging from the primary vertex. The recoil system X' is limited to the recoil nucleon plus de-excitation neutrons and photons. There is no limitation on the value of W.

For the analysis reported here, the selected event samples for reactions (1) and (2) are restricted by requiring all events to have hadronic mass W less than 1.8 GeV and neutrino energy in the range $1.5\,\mathrm{GeV} < E_\nu < 10\,\mathrm{GeV}$. Here, W is calculated from the true muon kinematics and true E_ν. Consequently the charged pion sample is nearly identical to the n-pion sample in Ref. [5] and the neutral pion sample is slightly smaller than in Ref. [6]. The restriction on final-state hadronic mass serves to enhance the contribution of $\Delta(1232)$ and N^* resonance production relative to that from CC DIS processes. Moreover the hadronic mass selection, together with the requirement that a Michel electron be observed on a non-muon track from the primary vertex, isolates a subsample of process (1) that is more nearly a π^+ production sample, as will be elaborated below.

The two separate CC pion production event samples were obtained with the NuMI beam in the low-energy mode, with the horn-current focusing set to produce a beam of predominantly ν_μ or $\bar{\nu}_\mu$. Consequently, the spectral shapes and effective E_ν range of the initiating $\nu_\mu/\bar{\nu}_\mu$ fluxes are similar for the two data sets. The initial studies measured the rates and kinematic distributions for the produced pions. Comparisons were made with generator predictions, and trends involving final-state interactions of the pions within the target carbon nuclei were identified. These measurements have also been compared to a phenomenological treatment of neutrino-induced pion production carried out within the GiBUU transport theoretical framework [7].

In the present work, the two CC(π) event samples are investigated further and in tandem, enabling the scope of Refs. [5] and [6] to be significantly extended. The present analysis encompasses the differential distributions of the final-state muon and of kinematic variables that are determined by the muon kinematics, with E_ν and Q^2 receiving particular attention. The resulting measurements are complementary to the pion kinematical distributions previously presented [5, 6]. While the distributions of these previous works show interesting sensitivity to the FSI processes, the distributions presented here depend on the combination of underlying pion-production reactions on single nucleons with nuclear medium effects arising from nucleon-momentum distribution and nucleon-nucleon correlations.

Comparisons of muon-related kinematic distributions are used to elicit similarities and differences between the ν-induced and $\bar{\nu}$-induced pion production datasets. To illuminate the contributing processes, each data distribution is also compared to predictions obtained using neutrino event generators. For the latter data-vs-simulation comparisons, the analysis makes use of three neutrino event generators that are widely used by neutrino experiments, namely GENIE 2.6.2 [8], NEUT 5.3.3 [9], and NuWro [10]. These codes have been independently constructed and validated; a summary of the phenomenological strategies and models used by each generator is given in Ref. [5].

The measurements of this work utilize event selections and improved flux estimations that differ from those used by Refs. [5, 6]. These modifications are discussed in Secs. II and III.

II. OVERVIEW OF THE EXPERIMENT

A. Beam, Detector, and Exposures

MINERvA uses a fine-grained, plastic-scintillator tracking detector [11] in conjunction with the magnetized MINOS near detector [12], to record interactions of neutrinos and antineutrinos from the high-intensity NuMI beam at Fermilab [13].

The measurements reported here use the MINERvA detector central tracking volume as the target, with the surrounding electromagnetic and hadronic calorimeters providing containment. The central volume has a hexagonal cross section of 2 m inner diameter, extends longitudinally for 2.5 m, and has a mass of 5400 kg. It consists of planes of polystyrene scintillator strips oriented perpendicular to the horizontal axis of the detector. The horizontal axis is inclined 3.3° relative to the beam axis. There are three scintillator-plane orientations, at 0° and ±60° relative to the detector vertical axis, that provide X, U, and V "views" of interactions in the scintillator medium. The module planes alternate between UX and VX pairs, enabling 3-D reconstruction of vertices, charged tracks, and electromagnetic showers of neutrino events. Separation of multiple interactions within a single 10 μs beam spill is made possible by the 3.0 ns timing resolution of the readout electronics.

The MINOS near detector, located 2 m downstream, serves as the muon spectrometer for the MINERvA central tracker. A muon exiting downstream of MINERvA is tracked by the magnetized, steel-plus-scintillator planes of MINOS, enabling its momentum and charge to be measured. The combination of position, angle, and timing in each detector allows matching of muon tracks in the two detectors. Full descriptions of the design, calibration, and performance of the MINERvA detector configuration are available in Refs. [11, 14].

The data were taken between October 2009 and April 2012 using the low-energy NuMI mode, which produces a wide-band beam with neutrino energies extending from 1 GeV to greater than 20 GeV and a peak energy of 3 GeV. The current-polarity of the magnetic horns in the beamline is set to focus either π^+ or π^-, providing ν_μ or $\bar{\nu}_\mu$ fluxes of approximately 92% purity or 40% purity respectively. The ν_μ CC charged-pion production events were obtained from an integrated exposure of 3.04×10^{20} protons on target (POT); the $\bar{\nu}_\mu$ CC single-π^0 production events were obtained in exposures with a total of 2.01×10^{20} POT. Half of the $\bar{\nu}_\mu$ exposure was taken with only the downstream half of the detector during construction. The two datasets are analyzed separately and the final results combined.

The ν_μ and $\bar{\nu}_\mu$ fluxes for these exposures were calculated using a detailed simulation of the NuMI beamline based on Geant4 [15, 16] and constrained by published proton-carbon yield measurements [17–19]. Compared to the previous studies, Refs. [5, 6], the measurements reported here benefit from improved flux predictions resulting from new constraints based upon $\nu + e^-$ elastic scattering data from MINERvA and from incorporation of new data on pion and kaon yields [20, 21]. Consequently the present work contains improved estimations for absolute event rates for each of the two data sets. All event-generator predictions are based upon the improved flux predictions. Updates to the previously published results [5, 6] using the new fluxes are presented in the Appendix of this paper.

B. Neutrino interaction modeling

Neutrino and antineutrino-nucleus interactions are simulated using version 2.6.2 of the GENIE neutrino event generator [8]. The generation of inelastic CC neutrino-nucleus interactions involves three different considerations:

- *Target nucleons:* Nucleons inside the nucleus are treated as a relativistic Fermi gas. The nucleon momentum distribution is augmented with a high-momentum tail [22] in order to account for short-range correlations. The possibility of neutrino interactions on correlated-nucleon pairs is not included.

- *The primary interaction:* Neutrino-induced pion production arising from a single struck nucleon can proceed either by baryon-resonance excitation or by non-resonant processes. The baryon-resonance pion production is simulated using the Rein-Sehgal model [23] with modern baryon resonance properties [24] and with an axial-vector mass of $M_A^{Res} = 1.12 \pm 0.22$ GeV [25]. For non-resonant pion production, GENIE uses the Bodek-Yang model [26] with parameters adjusted to reproduce the neutrino-deuterium bubble chamber measurements over the final-state invariant hadronic mass range $W < 1.7$ GeV. The GENIE implementation does not include the Rein-Sehgal treatment of baryon-resonance interference, nor does it carry along the lepton mass terms in the cross section calculations.

- *Intranuclear interactions of final-state hadrons:* Final-state interactions (FSI) of hadrons produced inside the nucleus with the nuclear medium are simulated. The FSI are especially important for pions because of the very large pion-nucleon cross sections in the $\Delta(1232)$ resonance region. In GENIE, an effective model for the FSI simulation is used in lieu of a full intranuclear cascade treatment. That is, pions can have at most one interaction on their way out of the nucleus [27]. This approximation works well for light nuclei such as carbon, the dominant target nucleus reported in this work. It is assumed that the pions produced inside the nucleus have the same pion-nucleus cross sections as

beam pions, and so scattering data from beam-pion measurements [28, 29] are used to model the interaction. The total interaction probability is determined by the pion-carbon total cross section. An interaction of a pion within the nucleus proceeds by one of four processes, namely pion absorption, inelastic scattering, elastic scattering, and charge exchange with probabilities according to the corresponding data. Kinematic distributions in the final state are set by algorithms that are fit to the corresponding pion-nucleus data.

Coherent pion production is different from other interactions because the neutrino interacts with the whole nucleus at once. Coherent single-pion production by CC interactions on carbon has been measured by MINERvA [30]. In GENIE, it is simulated according to the Rein-Sehgal model, updated with lepton mass terms [31].

C. Detector response

Simulation of the response of the MINERvA detector to particle propagation is provided by a Geant4-based model [15, 16]. The scale for muon dE/dx energy loss in the detector is known to within 2%. The scale is established by requiring agreement between data and simulation for the reconstructed energy deposited by momentum-analyzed, through-going muons. Hadron interactions in the detector materials are handled by the Geant4 QGSP_BERT physics list.

In order to reconstruct the energy of hadronic showers imaged by the detector, calorimetric corrections are required. The procedure whereby these corrections are determined from simulation is described in Ref. [11]. A scaled-down replica of the MINERvA detector, operated in a low-energy particle test beam, was used to establish the spectrometer's tracking efficiency and energy response to single hadrons, and to set the value for the Birks' constant of the scintillator [14]. The average deviation between data and GEANT4 for pions was 5%.

III. CC EVENT SELECTIONS AND RECONSTRUCTION

The 10 μs NuMI beam spill is divided into "time slices" that, based on the total visible energy in the scintillator as a function of time, encompass single events. As a charged particle traverses the scintillator strips of the detector, its trajectory is recorded as individual energy deposits (hits) having a specific charge content and time-of-occurrence. The hits are grouped in time, and then neighboring hits in each scintillator plane are gathered into objects called clusters. Clusters having more than 1 MeV of energy are then matched among the three views to create a track. The per-plane position resolution is 2.7 mm and the track angular resolution is better than 10 mrad [11] in each view.

A track that exits via the downstream surface of the MINERvA spectrometer and matches with a negatively-charged (positively-charged) track entering the front of MINOS near detector, is taken to be the $\mu^-(\mu^+)$ track of a CC event. The reconstruction of the muon tracks in this experiment (including both MINERvA and MINOS detectors) gives a typical momentum resolution of 6%. Muon track reconstruction incurs a small inefficiency due to event pileup. This effect is studied by isolating individual tracks in either of the MINERvA or MINOS detectors, projecting them to the other detector, and then measuring the rate of reconstruction failures. In this way it is determined that the simulated efficiency for muon reconstruction requires a correction of -4.4% (-1.1%) for muons with less than (greater than) 3 GeV/c.

A. Pre-selections; calculation of neutrino energy

Although the two data sets involve different beams and final-state particles, they have many features in common. In each case, reconstruction of CC event candidates proceeds by finding a long track that traverses both MINERvA and MINOS and treating it as the muon. The algorithm then searches for additional tracks that share a vertex with the longest track. Kinked tracks, which are usually the result of secondary interactions, are then reconstructed by searching for additional tracks starting at the endpoints of tracks previously found. The differences in acceptance between μ^- and μ^+ for the two samples are minor, and backgrounds from wrong-sign muons are insignificant in either sample. Since the signal reactions are different, there are of course differences in selection cuts, particle identification, and background subtraction procedures. However after the final sample is obtained with each data set, the analyses the same method to extract the cross section.

To be accepted as a candidate event, a muon neutrino (antineutrino) interaction must have a μ^- (μ^+) track and the muon must originate within the central tracking volume. The latter vertex is the primary interaction vertex; it is required to be the only interaction vertex within its time slice. Furthermore the interaction vertex must lie within the fiducial volume. For the neutrino (antineutrino) events analyzed here, their primary vertices must occur within the central 112 planes of the scintillator tracking region and must be at least 20.5 cm (22 cm) from any edge of the planes. The fiducial volume contains a target mass of 5.57 (5.37) metric tons with 3.54 (3.41) $\times 10^{30}$ nucleons.

The final-state muon momentum p_μ (and hence its energy E_μ) is reconstructed using the muon track's curvature or range measured in MINOS, in conjunction with the track's dE/dx energy loss from its observed traversal of the MINERvA spectrometer. The total final-state hadronic energy, E_H, is measured via calorimetry using the scintillator light outputs generated by the final-state hadron shower particles. More specifically, E_H is ob-

tained by scaling the calorimetric energy visible in the detector according to the Monte Carlo detector response. The neutrino energy E_ν is then calculated as follows:

$$E_\nu = E_\mu + E_H. \quad (3)$$

The resolution for E_ν determined in this way is 6%. Further analysis procedures for the two samples – their similarities and differences – are described below.

B. $\pi^\pm$ reconstruction; ν_μ-CC(π^+) selection

Events of the ν_μ-CC(π^+) sample must have a reconstructed μ^- track that is matched in the MINERvA and MINOS detectors, and the final state must have at least one charged pion track. Furthermore the reconstructed neutrino energy must be in the range 1.5 – 10 GeV and the invariant hadronic mass must be less than 1.8 GeV. There is no restriction on neutral pions, other mesons, or baryons. Charged-current coherent pion production is included in the signal definition. In practice, only $\sim$ 5% of selected events have more than one charged pion.

Charged particle tracks are reconstructed by applying two pattern recognition algorithms to the clusters found within the tracking volume and downstream calorimeters. Charged pion tracks are identified using a containment requirement plus two particle-identification selections [5]. This results in an estimation of particle type and a determination of kinetic energy, T_π.

A pion track is required to begin at the event vertex and to stop in either the tracking or electromagnetic-calorimeter regions of the central tracker. This requirement restricts the maximum pion kinetic energy to 350 MeV. The track is required to satisfy a particle-identification algorithm that evaluates the energy deposition pattern using the Bethe-Bloch formula and – very importantly – to have, in the vicinity of its endpoint, a candidate Michel electron from the $\pi^+ \to \mu^+ \to e^+$ decay sequence [5].

The Michel selection disfavors negatively-charged pions that tend to be captured on a nucleus before decaying, and discriminates strongly against pions that undergo charge exchange or absorption, thereby improving the pion energy resolution. The efficiency for finding pion tracks with $T_\pi > 50$ MeV in simulated CC($N\pi^\pm$) events (N = 1,2) with $W < 1.8$ GeV, is 42%. The primary reasons for pion tracking inefficiency are secondary interactions of the pion in the detector and activity in high-multiplicity events that obscures the pion.

The invariant mass cut is on the experimentally-determined hadronic invariant mass, W_{exp}. The cut was chosen to enrich the sample in events coming from baryon resonances; in addition, the reconstruction efficiency is higher because the final states have lower multiplicity. Singly-produced π^- tracks can only arise from FSI processes, and in any case the requirement that pion tracks of selected events have Michel electrons eliminates most of them. Consequently the selected pions are predicted to be π^+ at the level of 98.6%. The overall efficiency with which signal events having charged pions between 35 MeV and 350 MeV are selected is calculated to be 3%. This value reflects reductions incurred as the result of the MINOS-matched muon requirement, the pion track reconstruction inefficiency (42%), and the Michel electron selection. According to the GENIE-based Monte Carlo simulation for this analysis, the selected event sample has a signal purity of 86%.

Figure 1 shows a ν_μ + hydrocarbon data event from the ν_μ-CC(π^+) sample. Emerging from the primary vertex in the central, plastic-scintillator tracking region are a muon track that exits downstream, a charged pion, and a short, heavily ionizing proton. The projected image shows vertical and horizontal spans in the detector medium of approximately 2.0 m and 3.2 m respectively.

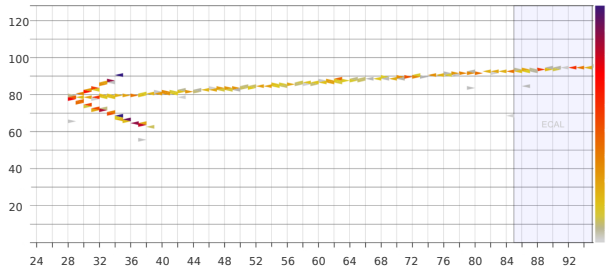

FIG. 1. Neutrino data event of the ν_μ-CC(π^+) sample from the top view. The neutrino enters from the left. The primary vertex occurs in the central scintillator tracking region; the muon traverses the downstream ECAL and HCAL regions and projects into the MINOS near detector (downstream, not shown). The event is a candidate for the final state $\mu^-\pi^+p$. The X and Y axis labels show the module and strip numbers. The color (online) linear scale (0 – 10 MeV) indicates the amount of energy deposited in the strips.

C. Selections for $\bar{\nu}_\mu$-CC(π^0)

For the $\bar{\nu}_\mu$-CC(π^0) sample, the events must have a reconstructed μ^+ track matched in the MINERvA and MINOS detectors, and the final state must contain a single π^0 unaccompanied by other mesons, with no restriction on the number of nucleons.

Candidate events contain a muon track in time coincidence with two electromagnetic showers. Tracks that start within 5 cm of the vertex are considered to come from the primary vertex. Events that have primary tracks other than the muon track are rejected. Also removed are events that have isolated tracks that do not point back to the vertex. Quite often, photons from the π^0 decays are reconstructed as tracks. Therefore, tracks with separation distance greater than 5 cm from and pointing back to the event vertex are not considered as coming from the vertex, and their associated energy clusters are made available to the π^0 reconstruction. The total visible energy in the tracker, electromagnetic

calorimeter (ECAL), and hadronic calorimeter (HCAL) is required to be greater than 80 MeV and less than 2 GeV. The cut on low visible energy removes events whose total energy deposition is too low to encompass the π^0 rest mass. The upper visible energy cut removes deep inelastic scattering (DIS) background events. Candidate events are allowed to have isolated hit clusters in the vicinity of the vertex because these may be induced by final-state nucleons interacting with the hydrogen or carbon nuclei of the detector. The data event shown in Fig. 2 is a $\bar{\nu}_\mu$ + hydrocarbon interaction that exhibits the prerequisite properties for retention in the $\bar{\nu}_\mu$-CC(π^0) candidate sample.

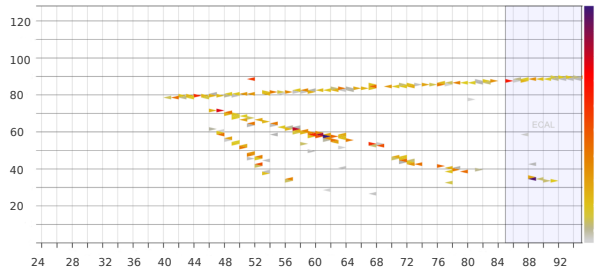

FIG. 2. Antineutrino data event and candidate for the final state $\mu^+\pi^0 n$ from the top view. The event is initiated in the central scintillator tracker and extends into the downstream electromagnetic calorimeter. It contains a μ^+ track accompanied by two photon showers.

Events that satisfy the topological selections are passed to the π^0 reconstruction. The reconstruction proceeds in two stages. In the initial stage pattern recognition is performed to identify the two gamma showers. Hit clusters found in the X view that are close in polar angle with respect to the vertex, but can be separated in radial distance from the vertex, are grouped into photon-conversion candidates. Then, for each candidate, clusters in the U and V views that are consistent among the three views are added. Photon candidates must have clusters in at least two views in order to enable their directions to be reconstructed in three dimensions.

Reconstruction of the photon showers is carried out in the second stage. The position, direction, and energy of a photon shower are determined by the clusters that have been assigned to each of the candidate photons. The photon direction is reconstructed from the cluster energy-weighted slopes in each view. The photon vertex is defined using the closest cluster to the event vertex on the photon direction axis. The photon energy is reconstructed by calorimetry using calibration constants determined by detector response simulations.

Candidate events must have exactly two reconstructed photon showers. In order to reduce charged-pion backgrounds, each photon is required to have converted at least 15 cm (0.36 radiation length) away from the primary vertex. The two-photon invariant mass $m_{\gamma\gamma}$ is reconstructed from the photon energies E_1, E_2 and the separation angle $\theta_{\gamma\gamma}$ between the two photons using

$$m^2_{\gamma\gamma} = 2E_1E_2(1-\cos\theta_{\gamma\gamma}). \quad (4)$$

The overall calibration constant that sets the absolute energy scale is determined by matching the peak in the $\gamma\gamma$ invariant mass distribution to the nominal π^0 mass. This procedure is done separately for data and simulation which enables correction for a difference in energy scales of 5% with 2.2% uncertainty between the data and simulation. Finally, the π^0 momentum is calculated from momentum conservation, $\vec{p}_{\pi^0} = \vec{k}_1 + \vec{k}_2$, where $\vec{k}_i$ are reconstructed photon momenta. The π^0 reconstruction typically has a 25% energy resolution and 3.5° angular resolution in each view.

It is required that the invariant mass $m_{\gamma\gamma}$ lies between 75 MeV/c^2 and 195 MeV/c^2, and that E_ν falls between 1.5 and 10 GeV. The lower cut on E_ν maximizes MINOS acceptance while the upper cut reduces flux uncertainties. Additionally, the reconstructed W is limited to $W < 1.8$ GeV.

D. Reconstruction of Q^2 and W

Calculation of the four-momentum-transfer-squared, Q^2, and of the hadronic invariant mass, W, proceeds according to

$$Q^2 = -(k-k')^2 = 2E_\nu(E_\mu - |\vec{p}_\mu|\cos\theta_\mu) - m^2_\mu, \quad (5)$$

and

$$W^2 = (p+q)^2 = M^2_N + 2M_N(E_\nu - E_\mu) - Q^2, \quad (6)$$

where p is the four-momentum vector of the initial nucleon, $q = k - k'$ is the four-momentum transfer, and M_N is the nucleon mass.

The calculations for E_ν (Eq. (3)) and Q^2 (Eq. (5)) do not involve any assumption concerning the state of the initial nucleon momentum or the composition of particles in the final state. On the other hand, the prescription for estimation of W in Eq. (6) assumes an initial-state nucleon at rest. The Monte Carlo uses a relativistic global Fermi Gas nuclear model; this model is known to be accurate for high momentum transfers (roughly $Q^2 > 1$ GeV^2) but less accurate for low momentum transfers. The rms widths of the Q^2 and W variables are 18% and 8%, respectively, for the charged pion analysis and 16% and 10% for the neutral pion analysis.

IV. DETERMINATION OF CROSS SECTIONS

After particle identification, the ν_μ-CC(π^+) sample contains 5410 events. For the full sample of signal events, the efficiency is 1.25% and the purity is 86%. The total background is estimated using the distribution of the reconstructed invariant mass, W_{exp}, shown in Fig. 3.

The largest contribution to the background (69%) is estimated to arise from pion production at true (simulation) hadronic invariant mass values, W_{true}, greater than 1.8 GeV. Events with protons misidentified as pions account for 19% of background, while events with $E_\nu > 10$ GeV, primary vertices outside the fiducial volume, and neutral current events account for the remaining 9%, 2%, and 1% respectively.

The selected $\bar{\nu}_\mu$-CC(π^0) sample contains 1004 events. The total selection efficiency is 6% and the purity is 55%. It is estimated that 70% of the total background is populated by antineutrino interactions that produce at least one π^0 in the detector. The background is nearly equally comprised of multi-pion production events, e.g. $\pi^0 + \pi^\pm$, where the $\pi^\pm$ is not tracked, and events with a secondary π^0 produced by $\pi^- \to \pi^0$ charge exchange or by nucleon scattering in the detector volume. The remaining 30% of background events are non-π^0 events wherein π^- and neutron-induced ionizations are mistakenly identified as photons.

A. Background subtraction and unfolding

Cuts are made in both analyses to focus on the response in the kinematic region dominated by baryon resonances ($W < 1.8$ GeV). However the W_{exp} cut described in Sect. III B is insufficient to get the desired measurement. A significant background comes from true pion production at higher W; for the selected charged pion sample this background comprises 6% of the sample. To remove this background, events are first selected with $W_{exp} < 1.8$ GeV with W calculated as in Sect. III D. Then, background is subtracted according to W_{true} (the value of W at the primary interaction according to the Monte Carlo) through a sideband procedure [32]. The $\bar{\nu}_\mu$-CC(π^0) analysis includes an additional background subtraction based upon the $m_{\gamma\gamma}$ spectrum.

For the background subtraction based upon W_{true}, the simulated W_{exp} distribution is divided into signal and background templates according to $W_{true} < 1.8$ GeV (signal) and $W_{true} > 1.8$ GeV (background) as indicated in Fig. 3a. The templates are then fitted, bin-by-bin, to the W_{exp} spectrum; the normalizations of the signal and background templates are the fit parameters in maximum likelihood fits (see Ref. [32] for details). The full W_{exp} spectrum after the fit is shown in Fig. 3b.

For the $\bar{\nu}_\mu$-CC(π^0) sample, the background is constrained using the two-photon invariant mass $m_{\gamma\gamma}$ distribution. Figure 4 shows the $m_{\gamma\gamma}$ distribution of the data and shows the contributions from signal and background that are estimated by the MC simulation. The data $m_{\gamma\gamma}$ distribution is fitted to a $m_{\gamma\gamma}$ model using the binned extended maximum-likelihood method. The model is constructed from the shapes of the MC signal and background event distributions. The expected numbers of signal and background events are parameters determined from the fit. The result of the fit is shown as solid histogram in the same figure. The fit reduces the background normalization in the signal region by 11% compared to the simulation prediction.

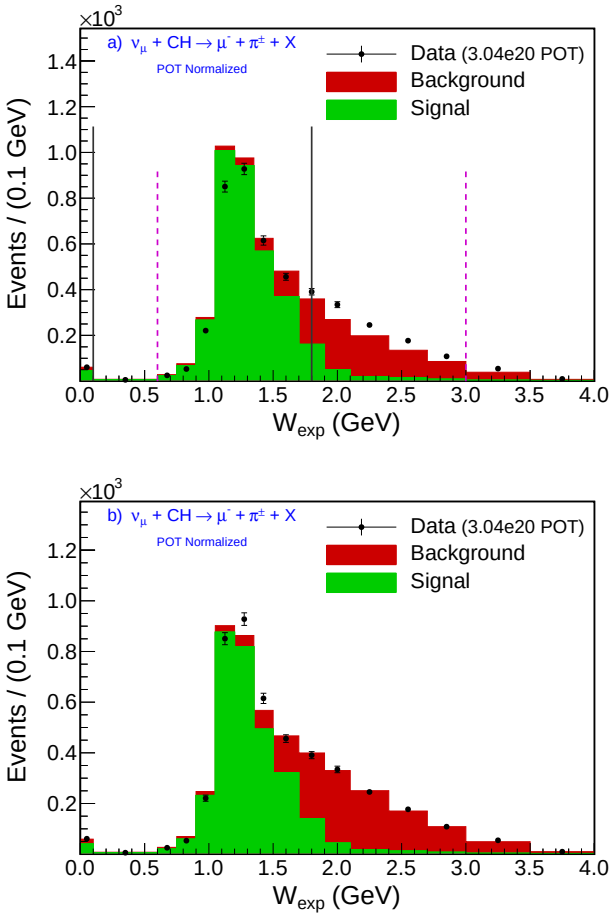

FIG. 3. The W_{exp} spectrum for the ν_μ-CC(π^+) sample comparing the data (solid points) to the Monte Carlo simulation (histograms) before (a) and after (b) the fit over the region between the vertical dashed lines in the upper plot. The Monte Carlo prediction is the sum of signal template (green online) and background template (red online) contributions. The analysis selects a signal-dominated sample (between the vertical solid lines) by requiring $W_{exp} < 1.8$ GeV.

Resolution effects in the scintillator are simulated with Monte Carlo and are unfolded from the data using a Bayesian procedure [33]. For either event sample, the unfolding matrices are close to diagonal and so the effects of unfolding are minor.

B. Cross section calculation

As in Refs. [5, 6], the flux-integrated differential cross section per nucleon for kinematic variable X (such as θ_μ,

p_μ, and Q^2), in bins of i, is calculated according to

$$\left(\frac{d\sigma}{dX}\right)_i = \frac{1}{T\Phi}\frac{1}{\Delta X_i}\frac{\sum_j U_{ij}\left(N_j^{data} - N_j^{bkg}\right)}{\epsilon_i}. \quad (7)$$

Here, T is the number of nucleons in the fiducial volume, Φ is the integrated flux, ΔX_i is the bin width, ϵ_i is the selection efficiency and acceptance. The unfolding function, U_{ij}, calculates the contribution to true bin i from reconstructed bin j, with the number of data candidates, N_j^{data}, and the number of estimated background events, N_j^{bkg}. Both the efficiency ϵ and the unfolding matrix U are estimated using the simulation. The total cross section in neutrino energy is calculated in a slightly different way:

$$\sigma(E_\nu)_i = \frac{1}{T\Phi_i}\frac{\sum_j U_{ij}\left(N_j^{data} - N_j^{bkg}\right)}{\epsilon_i}. \quad (8)$$

Here, the total flux Φ_i is calculated for each bin of neutrino energy. Both the integrated and binned fluxes are calculated by Monte Carlo methods which take into account the full geometry of the production target region and all processes by which pions and kaons are produced and subsequently decay.

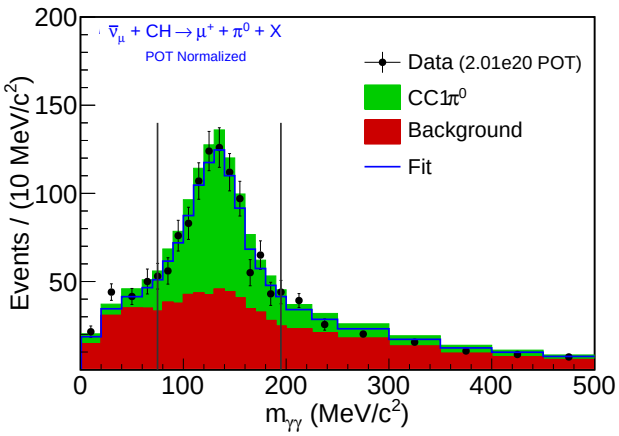

FIG. 4. Distribution of the invariant mass of the $\gamma\gamma$ pair. Data are shown as solid circles with statistical error bars. The shaded histograms show the Monte Carlo predictions for the $\bar{\nu}_\mu$-CC(π^0) signal and background. The solid blue (online) histogram is the maximum-likelihood best fit to the data. The vertical lines indicate the invariant mass cut, $75\,\mathrm{MeV/c^2} < m_{\gamma\gamma} < 195\,\mathrm{MeV/c^2}$, that defines the signal region.

The present analysis benefits from updated flux calculations [21]. In addition, a flux constraint provided by the MINERvA $\nu + e^-$ scattering measurement [20] has been applied. The constraint derived from measurement of muon-neutrino elastic scattering on electrons yielded a fractional change of between 1-2% in absolute rate for the range 1.5 GeV $< E_\nu <$ 10 GeV. Larger changes arose from revision of the absolute fluxes downward by 11-12% upon constraining them to hadron production data and incorporating improved determinations of the beamline geometry [21]. Together, these changes resulted in an upward shift of absolute event rate for the neutrino (antineutrino) exposure of 13% (12%) averaged over the analyzed E_ν range. In each event sample, changes to energy dependence introduced by the updated fluxes are small; the changes are almost entirely in absolute magnitude for all results except for the neutrino energy cross section.

The revisions to pion production differential cross sections reported in [5, 6] are sizable; the updated cross sections are given in the Appendix. The revised values fall beyond the 1σ flux uncertainties of 9% and 10% indicated by the earlier works, however they remain within the overall systematics uncertainty envelopes given in those works.

V. SYSTEMATIC UNCERTAINTIES

Systematic uncertainties are evaluated in almost identical ways for the two event samples analyzed here. The methods used are described in Ref. [5]. The systematic uncertainty from the neutrino flux is described in detail in Refs. [21, 34]. Although the uncertainties arise from many individual sources, they can be grouped into five categories as being associated with the detector energy response (*i*), with the principal-process models (*ii*) and final-state interaction models used by the reference Monte Carlo (GENIE) (*iii*), and with the neutrino flux (*iv*). Among the remaining odd-lot of sources designated as "other" (*v*), subtraction of background gives the largest uncertainty in either data set.

A. π^+ production

Cross-section uncertainties are shown for muon momenta of the ν_μ-CC(π^+) sample in Fig. 5a. Uncertainty from systematic sources slightly exceeds the statistical error for this sample. No single source dominates the systematic error. The largest contribution arises from the detector energy response, which is expected because the hadronic energy is measured by the energy deposited in scintillator layers. The uncertainty in the neutrino flux is smaller than was the case for Refs. [5, 6], but it is still the second-largest source of uncertainty. The uncertainty associated with neutrino cross sections is somewhat smaller than the flux uncertainty.

B. π^0 production

Figure 5b shows the cross-section uncertainties for muon momenta of the $\bar{\nu}_\mu$-CC(π^0) sample. For this sample, the the statistical uncertainty of the limited data set (dashed histogram) is larger than either the flux or

cross-section uncertainties. The normalization of the background fit contributes 8% to the systematic uncertainty. Significant uncertainty arises from the misidentification of neutrons as photons. This source of error was evaluated by changing the neutron inelastic cross section within an error range based upon compiled measurements. A large fraction of the secondary π^0 in the background is estimated to arise from $\pi^- \to \pi^0$ charge exchange (CEX), for which the cross sections are poorly known. The effect of this uncertainty on our measurement is evaluated by changing the CEX cross section within its uncertainty of $\pm 50\%$ [28, 35, 36], and then re-measuring the cross sections. The uncertainty in the electromagnetic energy scale contributes 2.2% to the error budget, estimated from the fitted mean uncertainty of the data $m_{\gamma\gamma}$ distribution.

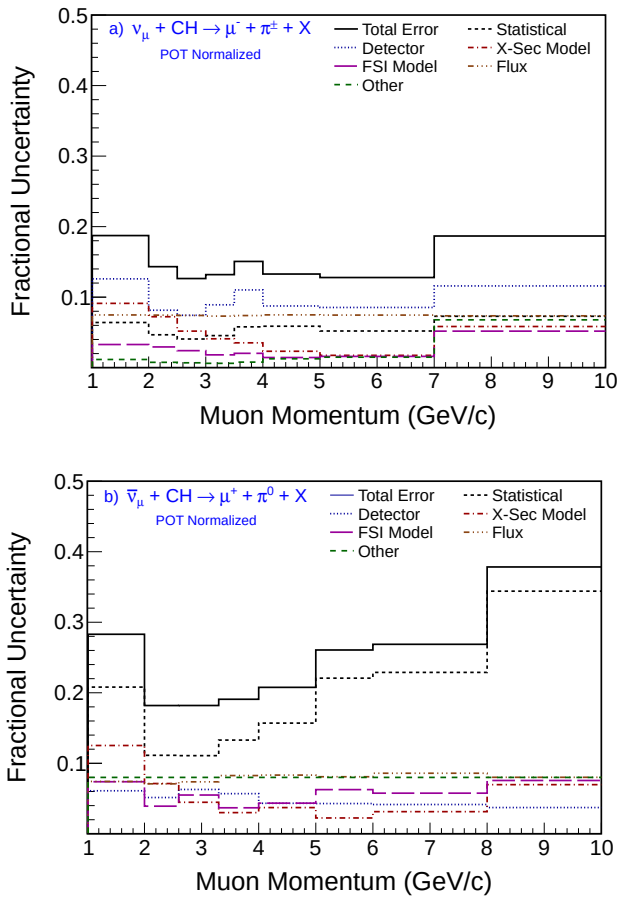

FIG. 5. Fractional uncertainties for muon momenta in the ν_μ-CC(π^+) analysis (a), and the $\bar{\nu}_\mu$-CC(π^0) analysis (b), for the case of absolute normalization to the data exposure. The statistical (total) error is shown by the dashed (highest solid-line) histogram in each plot. Component histograms show the contributions from the five systematic error sources.

The principal-interaction cross-section model (GENIE) also contributes significantly to the uncertainty of both analyses. One of the large uncertainties arises from modeling the basic pion production process on individual nucleons. Tables of values of the cross section and of systematic uncertainty decomposition for each bin of each measurement are given in the Supplement to this paper [37].

VI. MUON KINEMATICS IN CC(π) PRODUCTION

A. Muon production angle

Figure 6 shows the differential cross sections as a function of polar angle, θ_μ, with respect to the neutrino beam, for the ν_μ-CC(π^+) sample (Fig. 6a) and for the $\bar{\nu}_\mu$-CC(π^0) sample (Fig. 6b). For both samples, the θ_μ distribution peaks around 8° and then decreases gradually. Beyond 25° the acceptance into the MINOS near detector is small, and so no cross sections are given for that region. The superimposed solid-line (dashed-line) histogram shows the GENIE prediction that includes (omits) the intranuclear FSI treatment. The ratio of the predictions with/without FSI is observed to be roughly constant over the observed angular range.

Comparison of the dashed and solid-line histograms in Fig. 6a,b shows that pion FSI play a significant role in the GENIE predictions. In the ν_μ-CC(π^+) sample (upper plot), $\Delta(1232)$ production in the charge state Δ^{++} dominates the final state, and pion intranuclear absorption plus pion charge exchange deplete the number of final-state pions that exit the nucleus. This depletion cannot be compensated by charge-exchange feed-in from Δ^+ channels which are produced at lower rates (due to their smaller isospin amplitudes). Thus, for reactions (1), the GENIE prediction with FSI included is always smaller than the GENIE prediction without FSI. For reactions (2) of the $\bar{\nu}_\mu$-CC(π^0) sample however, the situation is reversed. The latter reactions also lose pions to intranuclear absorption and charge exchange. However, the feed-in of charge-exchanged π^0 originating from production of Δ^- states is always larger than the losses. Production of the latter states benefits from having a relatively large isospin amplitude. The net result is that for reactions (2) the GENIE prediction is elevated by the inclusion of FSI processes (Fig. 6b).

Differences in absolute rate between the data and GENIE predictions are evident in Fig. 6a. The GENIE prediction with FSI (solid-line curve) is too high by 20% to 30% for the neutrino-induced sample of Fig. 6a. On the other hand, Fig. 6b shows the GENIE prediction with FSI to be in good agreement with the distribution for the antineutrino sample. The uncertainties associated with the absolute ν_μ and $\bar{\nu}_\mu$ fluxes are 8.5% and 8.0% respectively, so the data/MC normalization differences are of order $2.4\,\sigma$ and $0.3\,\sigma$.

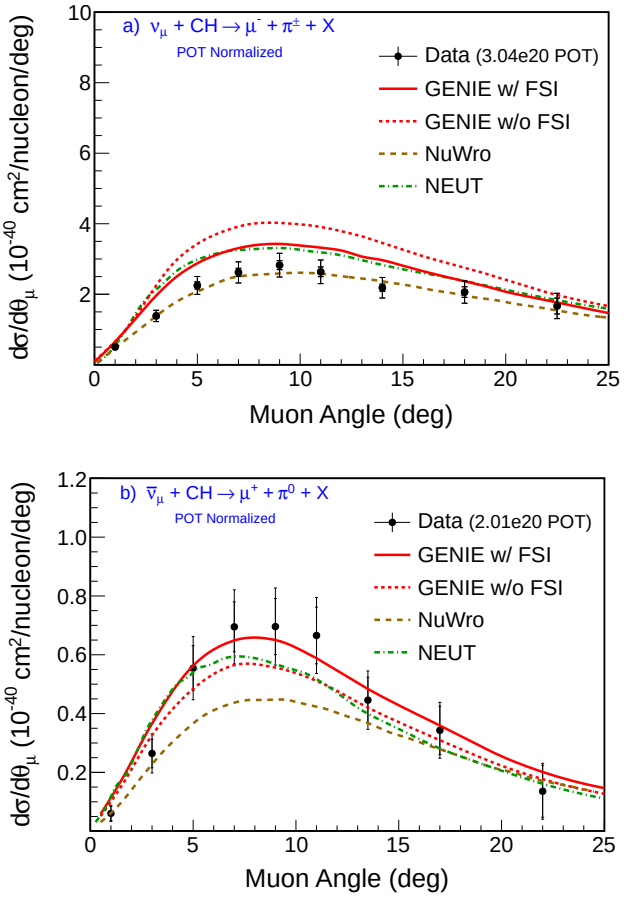

FIG. 6. Differential cross sections as a function of the muon production angle θ_μ for the ν_μ (a) versus $\bar{\nu}_\mu$ (b) pion production samples. Data are shown as solid circles. The inner (outer) error bars correspond to statistical (total) uncertainties. The solid (dashed) distributions are GENIE predictions with (without) FSI. Predictions for the NuWro and NEUT event generators are also shown.

In Fig. 6 and in subsequent figures, predictions of the NEUT and NuWro neutrino event generators are displayed with FSI effects included, providing comparisons with GENIE as well as additional predictions for the data. For baryon-resonance production, NEUT (like GENIE) uses the Rein-Sehgal model [23] but without inclusion of baryon-resonance interference, whereas NuWro includes only $\Delta(1232)$ production as formulated by the Adler model [38, 39]. NEUT also incorporates nonresonant pion production from Rein-Sehgal, whereas NuWro (like GENIE) uses the Bodek-Yang model [26] above the resonance region and extrapolates it to lower W so as to converge with the predictions of Rein-Seghal. For their FSI treatments, both NEUT and NuWro use the Salcedo-Oset model [40] in a cascade formalism that includes nuclear medium corrections. The NEUT and NuWro predictions are compared to data for which the background estimates have been launched from predictions of the GENIE event generator. The GENIE predictions however are constrained by data in the sidebands; moreover the full systematics uncertainties arising from GENIE as well as other sources are taken into account in the predicted backgrounds. Consequently any biasing of measurements towards GENIE predictions will fall within the systematics error envelope indicated for the data points.

Figure 6 shows that all three event generators achieve good agreement for the shape of $d\sigma/d\theta_\mu$ for both of the CC pion production samples. NEUT, like GENIE, predicts an absolute rate for the ν_μ-CC(π^+) sample that is distinctly higher than for the data, while the NuWro prediction for the same sample is in excellent agreement with respect to distribution shape and normalization. For the $\bar{\nu}_\mu$-CC(π^0) sample of Fig. 6b, however, the situation is opposite: GENIE and NEUT achieve good agreement in normalization as well as shape, while the NuWro prediction falls well below the data.

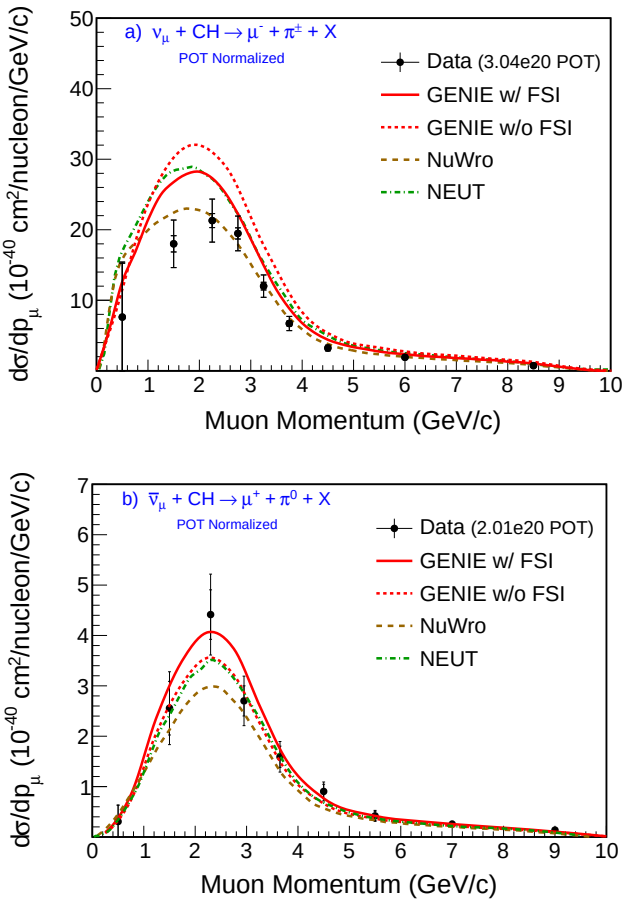

FIG. 7. Differential cross sections as a function of the muon momentum for the ν_μ (a) and $\bar{\nu}_\mu$ (b) pion production samples. Data are shown as solid circles. The inner (outer) error bars correspond to statistical (total) uncertainties. The solid (dashed) distributions are GENIE predictions with (without) FSI. Also shown are predictions for the NuWro and NEUT event generators.

Normalization differences between data and predictions of event generators can be driven by cross-section

uncertainties for $\nu_\mu/\bar{\nu}_\mu$ -induced pion production in scattering on free nucleons, as well as by flux uncertainties. The data constraining these processes are sparse, and in the case of $\nu_\mu + p \to \mu^- + \pi^+ + p$, the two bubble chamber measurements using 0.5 to ~ 3 GeV neutrinos reported cross sections that differed by $\sim 30\%$ in absolute normalization [41, 42]. (A recent reanalysis obtains consistency between these two data sets [43] , however the generator predictions shown here have not been tuned to the results of this reanalysis.) For the channel $\bar{\nu}_\mu + p \to \mu^+ + \pi^0 + n$ there is only one cross-section data point, obtained with antineutrino scattering on a heavy-liquid (freon CF_3Br) bubble chamber fill [44].

B. Muon momentum

The differential cross sections as a function of the muon momentum p_μ for the two samples are shown in Fig. 7. The distributions peak between 2.0 and 2.5 GeV and fall off rapidly as p_μ increases from 3.0 to beyond 6.0 GeV. The same trends as observed in $d\sigma/d\theta_\mu$ are apparent here in $d\sigma/dp_\mu$. The relatively large uncertainty for the lowest-momentum bin in Fig. 7a is an artifact of the muon acceptance in MINOS. Because muons with $p_\mu < 1$ GeV have low efficiency, the data selection requires $E_\nu > 1.5$ GeV. Therefore, the first bin only receives event counts as the result of the unfolding procedure.

Figure 7 compares the observed $d\sigma/dp_\mu$ distributions to predictions of the three event generators. Similar to the situation with $d\sigma/d\theta_\mu$ in Fig. 6, the three generators achieve good agreement with respect to the shape of $d\sigma/dp_\mu$ for both samples, but with variance in the predictions for absolute rates.

VII. COMPOSITION OF DATA SAMPLES

The event generators predict that several processes contribute to the event samples analyzed here. The GENIE prediction, for example, consists of quasielastic scattering, baryon resonance production, non-resonant pion production, DIS, and coherent pion production. For the pion production samples of this work, the topology selections and W restriction ensure that the contributions from quasielastic and DIS scattering are negligible. The samples are predicted to be dominated by single-pion final states arising from production and decay of the $\Delta(1232)$ and higher mass resonances, together with pion-nucleon non-resonant production. Figures 8 and 9 show the reaction-category composition for $d\sigma/d\theta_\mu$ and $d\sigma/dp_\mu$ of the ν_μ-CC(π^+) and $\bar{\nu}_\mu$-CC(π^0) samples. Referring to the component histograms, the ν_μ-CC(π^+) sample (Figs. 8a and 9a) is estimated by GENIE to be comprised $\approx 50\%$ of $\Delta^{+,++}$ production, followed by non-resonant pion production, and production of higher mass N^* states. For the $\bar{\nu}_\mu$-CC(π^0) sample (Figs. 8b and 9b), the Δ^0 is also prominent, however the higher-mass N^* contribution exceeds non-resonant pion production.

A recent paper [45] presents a new fit to the reanalyzed ν_μ-deuterium pion production data [43]. The best fit for GENIE 2.6.2 produces an increase in the resonant strength of about 15% and the non-resonant strength was decreased by about 50%. Those changes would produce better agreement between GENIE and the charged pion data shown in Figs. 8a and 9a.

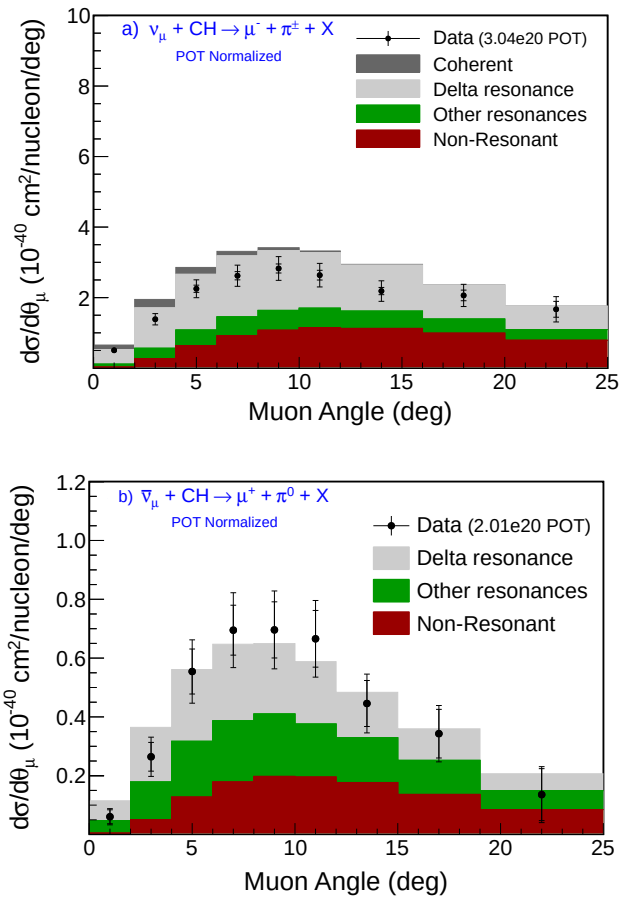

FIG. 8. Differential cross sections $d\sigma/d\theta_\mu$ as in Fig. 6 for the ν_μ (a) and $\bar{\nu}_\mu$ (b) pion production samples, showing the decomposition of the GENIE predictions into component reaction processes. The three dominant processes (histograms, bottom to top) are $\Delta(1232)$ production, higher-mass N^* production, and pion non-baryon-resonance production.

The ν_μ-CC(π^+) sample receives a small contribution from CC coherent single pion production. The GENIE prediction for this contribution is shown by the component at small θ_μ values in Fig. 8a (top, dark-shade histogram). Recall that in CC coherent pion production, the quantum (e.g. a pomeron) transferred to the struck nucleus carries no quantum numbers. The possible CC(π) coherent reactions are:

$$\nu_\mu(\bar{\nu}_\mu) + \mathcal{A} \to \mu^-(\mu^+) + \pi^+(\pi^-) + \mathcal{A} \; . \qquad (9)$$

For coherent scattering to occur, the muon-pion system must have zero electric charge (like the incident $\nu/\bar{\nu}$). Thus coherent CC(π) scattering is confined to the ν_μ-CC(π^+) sample; production of single π^0 mesons cannot occur via CC coherent $\nu/\bar{\nu}$ scattering.

Figure 8a shows coherent CC(π) scattering to be the only component process having a pronounced dependence on muon angle. The three dominant processes are spread fairly uniformly over the angular range, although the production of $\Delta(1232)$ is predicted to gain prominence at very forward θ_μ values. On the other hand, Fig. 9a indicates that all of the component processes, including coherent CC(π^+) scattering, distribute broadly with respect to muon momentum.

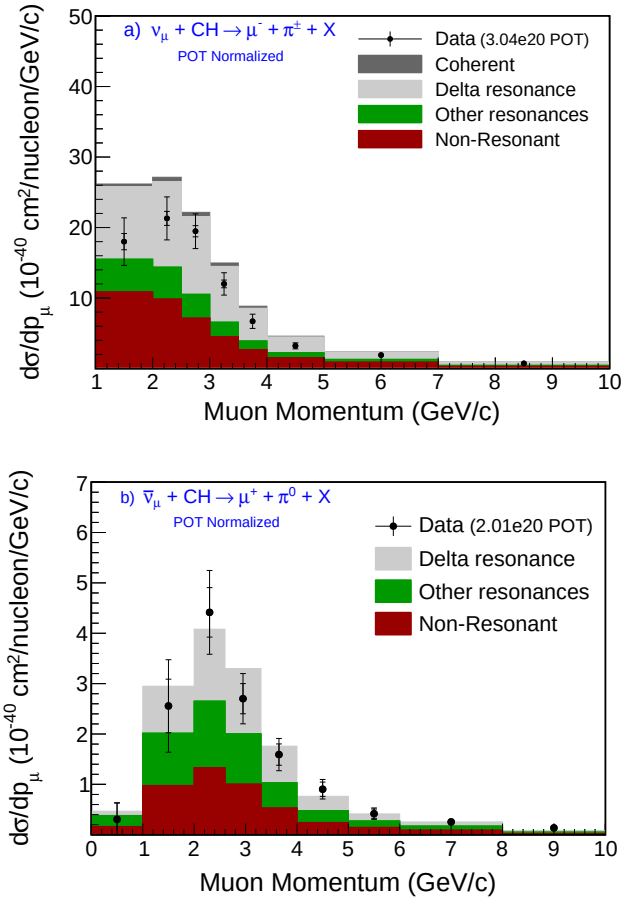

FIG. 9. Differential cross sections $d\sigma/dp_\mu$ as in Fig. 7 for the ν_μ (a) and $\bar{\nu}_\mu$ (b) pion production samples, showing the decomposition of the GENIE predictions into component reaction processes. The component processes are seen to distribute fairly uniformly with respect to muon momentum.

VIII. CC(π) CROSS SECTIONS VERSUS E_ν

Figure 10 shows the cross sections as functions of neutrino (antineutrino) energy for the ν_μ-CC(π^+) sample (upper) and for the $\bar{\nu}_\mu$-CC(π^0) sample (lower plot). Worthy of note is the difference in the ordinate ranges for the two plots. For the highest E_ν bin measured in each sample ($\langle E_\nu \rangle = 9.0$ GeV), the cross section for ν_μ-CC(π^+) is more than twice as large as the $\bar{\nu}_\mu$-CC(π^0) cross section. Also clearly discernible is the difference in the cross section rise-with-E_ν for the two samples. The cross section for ν_μ-CC(π^+) sample (Fig. 10a) reaches its plateau at $E_\nu \geq 3.0$ GeV. However, the cross section for $\bar{\nu}_\mu$-CC(π^0) (Fig. 10b), exhibits a gradual rise throughout the measured region $1.5 \leq E_\nu \leq 10.0$ GeV.

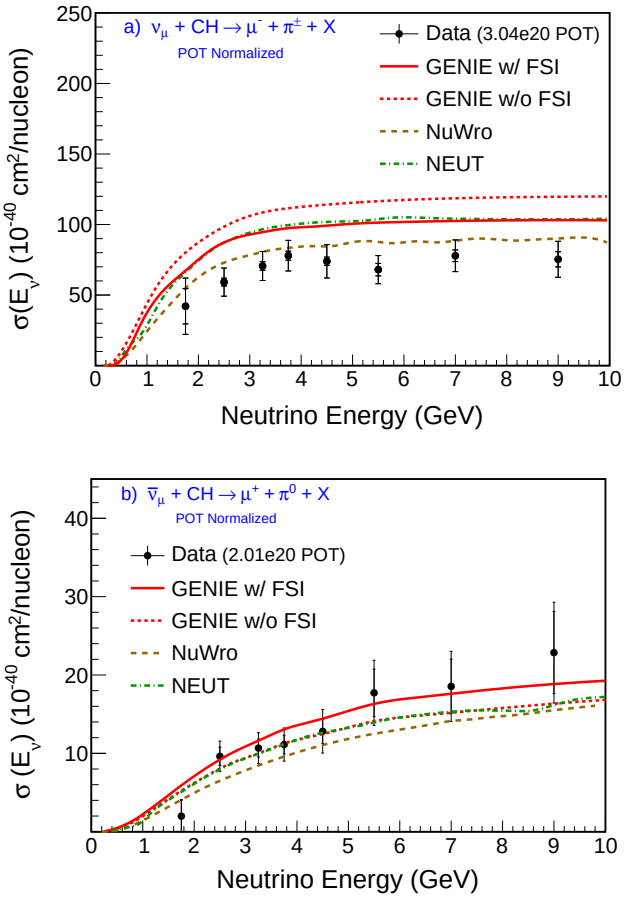

FIG. 10. Cross sections as a function of the neutrino energy E_ν for the ν_μ (a) and $\bar{\nu}_\mu$ (b) pion production samples. Data are shown as solid circles. The inner (outer) error bars correspond to statistical (total) uncertainties. The solid (dashed) distributions show GENIE predictions with (without) FSI, the long-dashed distribution is the prediction from the NuWro generator, and the dot-dashed distribution is the prediction from NEUT generator.

The relative trends are a manifestation of the underlying vector minus axial-vector ($V-A$) structure of the hadronic currents of these semileptonic weak interactions. Within the structure functions of antineutrino CC scattering, the $V-A$ interference terms have opposite sign compared to corresponding terms in the structure functions of neutrino CC scattering. The $V-A$ terms interfere destructively in the hadronic currents of

$\bar{\nu}_\mu$-CC scattering, whereas the interference is constructive in ν_μ-CC interactions. The interferences contribute significantly to the cross sections in the sub-GeV to few GeV range of E_ν and they account for the different trends in evolution with E_ν observed in Fig. 10a,b [23].

Figure 10 compares the measured cross sections to the predictions of GENIE, NEUT, and NuWro. The predictions for all of these generators exceed the measured ν_μ-CC(π^+) cross section, with GENIE and NEUT exhibiting a much larger disagreement (Fig. 10a). For the $\bar{\nu}_\mu$-CC(π^0) cross section (Fig. 10b), there is less variation among the generator predictions and much better agreement with the data.

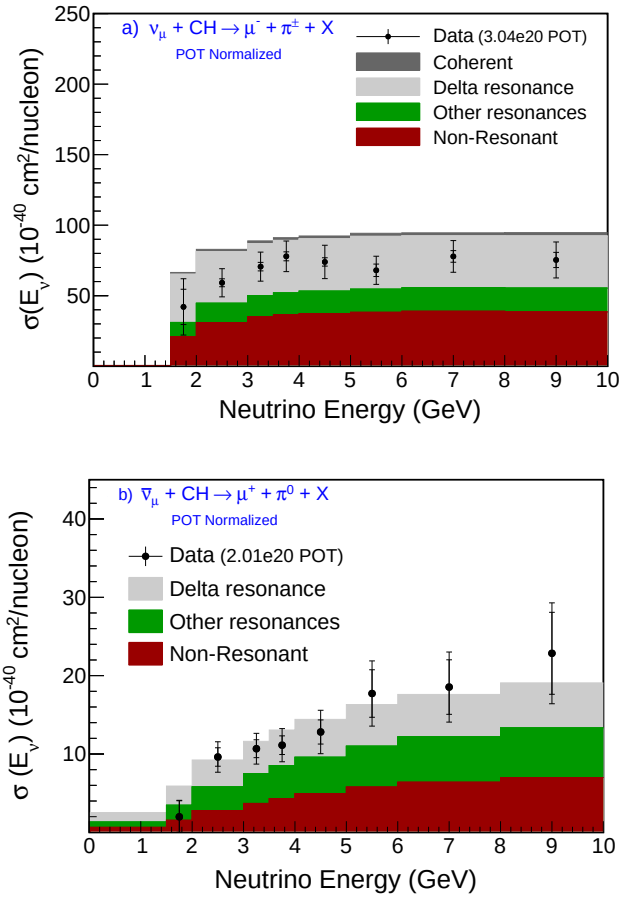

FIG. 11. Component reaction processes in GENIE cross-section predictions for the ν_μ-CC(π^+) (a) and $\bar{\nu}_\mu$-CC(π^0) (b) samples. Stacked histograms (bottom to top) show the contributions from *(i)* pion non-resonance processes, *(ii)* N^* states above the $\Delta(1232)$, and *(iii)* $\Delta(1232)$ resonance production.

Figures 11a,b show the component reaction processes that are included in the GENIE predictions for cross sections of the ν_μ-CC(π^+) and $\bar{\nu}_\mu$-CC(π^0) samples, respectively. Notably absent are dramatic changes in the mixture of components with increasing E_ν. Although the $\Delta(1232)$ resonance is expected to dominate at low E_ν in all models, its relative contribution would be expected to decrease at higher E_ν where more energy is available to excite the struck nucleon. The W cut at 1.8 GeV however mitigates such an effect. The pion non-resonant processes feature prominently in the GENIE predictions for both cross sections. The separation into resonant and non-resonant processes is model dependent and could be different in other models.

IX. $d\sigma/dQ^2$ OF CC(π) REACTIONS

The differential cross sections as a function of Q^2 for the ν_μ-CC(π^+) and $\bar{\nu}_\mu$-CC(π^0) samples are shown in Fig. 12. Note the large difference in the ordinate scales for the two distributions in corresponding Q^2 bins.

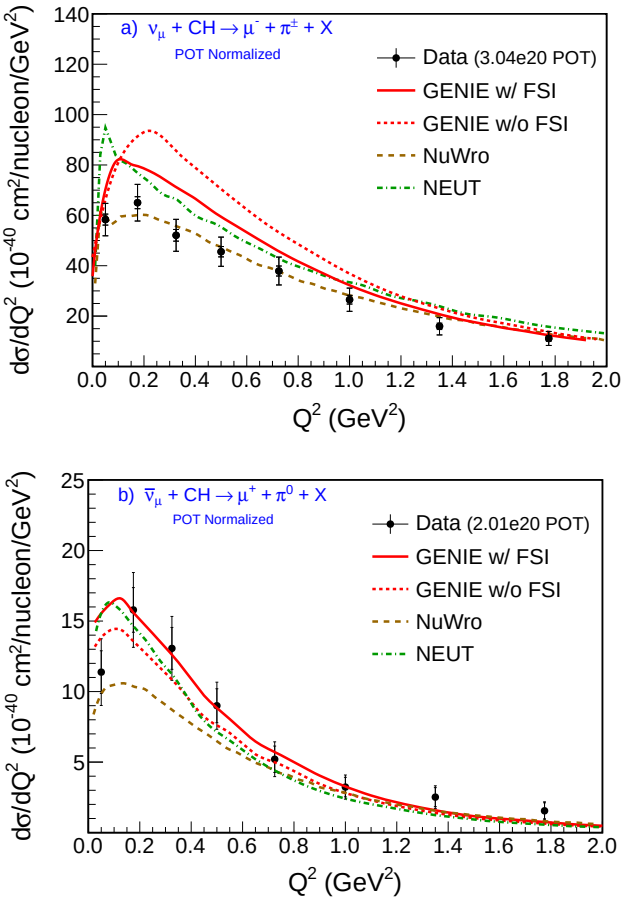

FIG. 12. Differential cross sections in four-momentum transfer squared Q^2 for the ν_μ-CC(π^+) sample (a) and the $\bar{\nu}_\mu$-CC(π^0) sample (b). Data are shown as solid circles. The solid (dashed) distributions are GENIE predictions with (without) FSI, shown together with predictions from the NuWro and NEUT event generators. Ordinate-scale difference reflects the larger cross section for the ν_μ-CC(π^+) sample.

For the generator predictions displayed in Fig. 12, NEUT and GENIE use a relativistic global Fermi gas model for nucleon momentum, while NuWro uses a local Fermi gas model. The three calculations have very

similar shapes for $Q^2 > 0.2$ GeV/c^2. At the lowest Q^2, it is possible that nucleon-nucleon correlations and Pauli blocking may contribute. These effects have been studied theoretically and experimentally in quasielastic neutrino scattering [46, 47].

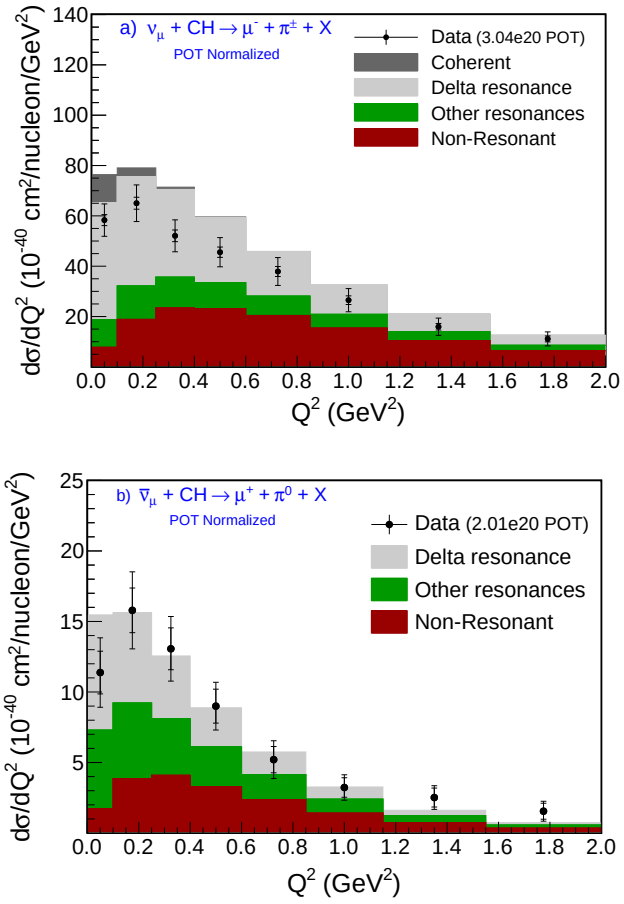

FIG. 13. GENIE reaction processes for the $d\sigma/dQ^2$ data distributions for the ν_μ-CC(π^+) (a) and $\bar{\nu}_\mu$-CC(π^0) (b) samples. The coherent scattering contribution to ν_μ-CC(π^+) is localized at very low Q^2.

Other effects can modify the cross section in Q^2 bins below 0.20 GeV^2. Recall that coherent scattering can contribute to ν_μ-CC(π^+) but not to $\bar{\nu}_\mu$-CC(π^0). By its nature, coherent scattering involves a very small four-momentum transfer to the target nucleus and so its contribution is confined to very low Q^2. Different models are commonly used; while NEUT and GENIE use different implementations of the Rein-Sehgal [31] model, NuWro uses the Berger-Sehgal [48] model. NEUT predicts a distinctly larger rate for coherent reaction (9) than does GENIE. Consequently the NEUT prediction (Fig. 12a) peaks near $Q^2 \simeq 0.0$ GeV^2, while GENIE and NuWro do not predict such an effect. In fact, GENIE and NuWro predict a mild turnover in $d\sigma/dQ^2$ as Q^2 approaches zero GeV, in agreement with the turnover exhibited by the data. MINERvA has published total cross section data for coherent pion production [30] using the same initial data samples as the analyses presented here. The NEUT prediction for the total coherent cross section is much larger than those data, while the GENIE prediction roughly agrees with the measured cross section in both shape and absolute rate.

Figure 13 shows the GENIE predictions for the sample compositions compared to the $d\sigma/dQ^2$ data points. The three main reaction categories are predicted to distribute broadly over the range $0.0 \leq Q^2 \leq 2.0$ GeV^2. The coherent scattering contribution to the ν_μ-CC(π^+) sample is predicted to be mostly confined to $Q^2 < 0.4$ GeV^2. At high Q^2, the non-resonant processes in GENIE have a larger contribution to the data than the baryon resonance processes. In Figs. 13a,b the GENIE predictions exhibit the same trends as observed in Figs. 8, 9, and 11, namely good agreement with the $\bar{\nu}_\mu$-CC(π^0) data and an absolute normalization that is high relative to the ν_μ-CC(π^+) data.

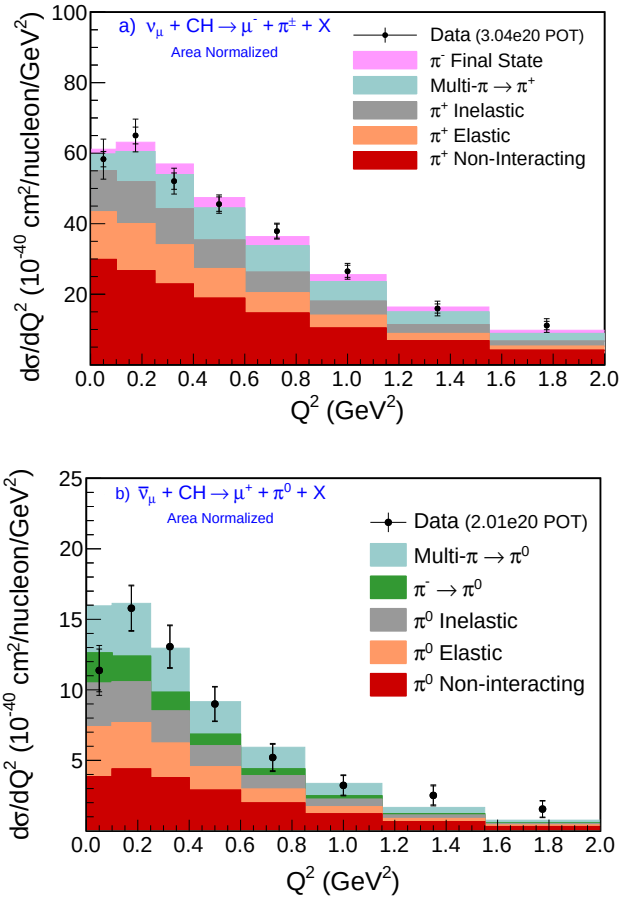

FIG. 14. Breakout of pion FSI processes within GENIE cross-section predictions for the two analysis samples. Stacked histograms (top to bottom) show contributions from π^- (for the charged pion sample), multiple-pion production with absorption, charge exchange (for the π^0 sample), inelastic scattering, elastic scattering, and no interaction. The full simulation, shown area-normalized to the data, reproduces the shape of data $d\sigma/dQ^2$ without ascribing Q^2-dependence to pion FSI.

Figure 14 shows a decomposition of the GENIE predictions according to pion FSI processes. Here, the simulation has been area-normalized to the data to better examine whether shape effects are present that could be related to FSI. The information displayed is complementary to that shown in Fig. 13. While Fig. 13 gives the GENIE subdivision by the primary process, Fig. 14 shows the subdivision by what happens after the primary process. For the pion kinematic variables [5, 6], the FSI processes are important in determining the shape of the distributions. However, for variables that are largely determined by form-factor dependence and the nuclear model (such as Q^2), pion FSI processes are expected to have a relatively mild affect. Referring to Fig. 12, the GENIE-based predictions that omit or include FSI (dotted versus solid curves), indicate that FSI processes reduce the differential cross section for ν_μ-CC(π^+) and elevate the differential cross section for $\bar{\nu}_\mu$-CC(π^0). The same trends are predicted by GENIE of the muon kinematic distributions of Figs. 6 and 7, and for the cross sections as functions of neutrino energy in Fig. 10.

The data for $\bar{\nu}_\mu$-CC(π^0) in Figs. 12b, 13b, and 14b (where coherent pion production cannot contribute) suggest a stronger turnover near $Q^2 \simeq 0.0$ than is predicted by the generators. This could be due to long-range nucleon-nucleon correlations, usually treated via the Random Phase Approximation (RPA) [46, 47], or to Pauli blocking. Pauli blocking should be applied for nonresonant pion production. Pion production through an intermediate $\Delta(1232)$ resonance should be subject to Pauli blocking, as $\Delta(1232)$ decay deposits a nucleon into the residual nucleus. The net effect is suppression of reactions at very low Q^2, similar to the suppression observed with neutrino quasielastic scattering. The Pauli blocking effect has been calculated for $\mu^\pm\Delta(1232)$ channels produced in carbon-like nuclei in Ref. [49]; the suppression is confined to $Q^2 < 0.2$ GeV^2 and to $W < 1.4$ GeV. The generator models shown here do not include any of these effects for pion production.

X. CONCLUSIONS

Differential cross sections in muon kinematic variables θ_μ and p_μ are reported and compared for pion production processes ν_μ-CC(π^+) and $\bar{\nu}_\mu$-CC(π^0) obtained by exposing hydrocarbon to ν_μ and $\bar{\nu}_\mu$ beams having similar flux profiles. Measurements of muon production angle and momentum are used to extract cross sections as functions of E_ν and of Q^2 for the pion production processes. Events with total hadronic mass $W < 1.8$ GeV are selected to emphasize the baryon resonance region. Together with the previous publications based on the same data sample [5, 6], these measurements provide a broad picture of pion production for neutrino energies 1.5 – 10 GeV wherein charged-current scattering from single nucleons is convolved with nuclear structure and pion FSI effects. Data summary Tables for the measurements of this work that may facilitate phenomenological investigations, are available in the Supplement [37].

The ensemble of differential cross sections are compared to simulations based upon the GENIE, NEUT, and NuWro event generators. For differential cross sections measured with the ν_μ-CC(π^+) sample, the absolute event rates predicted by GENIE and NEUT are observed to exceed the measurements of this work by amounts that are typically between 1-to-2 σ of the data. GENIE and NEUT predictions give much better agreement for the $\bar{\nu}_\mu$-CC(π^0) comparisons. On the other hand, the NuWro generator obtains agreement with the distributions for the ν_μ-CC(π^+) sample, but predicts event rates that are generally low by up to 1.5 σ relative to the data for $\bar{\nu}_\mu$-CC(π^0). The differences in generator predictions arise from differences in the cross section for pion production on free nucleons [45], and from the treatment of FSI, which has significant uncertainties. In contrast to the assorted discrepancies for absolute rates, all three generators obtain respectable shape agreement with the full suite of differential cross sections.

The suite of differential cross sections for the two samples is examined in light of the reaction category composition used by the GENIE generator. The likely role of coherent CC(π^+) scattering in the ν_μ-CC(π^+) sample is thereby illustrated. Comparisons of the three generators with $d\sigma/dQ^2$ for this sample indicates that the rate of coherent CC(π^+) is set too high in NEUT. The $d\sigma/dQ^2$ distribution of ν_μ-CC(π^+) has sensitivity to nuclear structure. Neither Pauli blocking nor nucleon-nucleon correlations are included in the default options of the GENIE, NuWro, or NEUT versions used here. Despite the simplicity of the nuclear models employed by these generators, the shapes of the Q^2 distributions predicted by GENIE and NuWro agree with the data.

In summary, the measurements and event sample comparisons of this work shed light on CC pion production by neutrinos and antineutrinos. A correct description of these data requires accurate models for this multifaceted problem. Separate understanding of the three aspects (pion production from the bound nucleon, nuclear structure, and pion FSI) are important for interpreting events recorded by the neutrino oscillation experiments at long baselines. Fortunately, the complete data set allows for some separation of processes. The measurements illuminate shortfalls in current generators with respect to absolute rate predictions for coherent, resonant, and non-resonant CC production of pions. These results can guide the development of improved neutrino-interaction models that are important to the international effort to obtain precision measurements of neutrino oscillations using ν_μ and $\bar{\nu}_\mu$ beams.

ACKNOWLEDGMENTS

This work was supported by the Fermi National Accelerator Laboratory under US Department of Energy

contract No. DE-AC02-07CH11359 which included the MINERvA construction project. Construction support was also granted by the United States National Science Foundation under Award PHY-0619727 and by the University of Rochester. Support for participating scientists was provided by NSF and DOE (USA), by CAPES and CNPq (Brazil), by CoNaCyT (Mexico), by CONICYT (Chile), by CONCYTEC, DGI-PUCP and IDI/IGI-UNI (Peru), and by Latin American Center for Physics (CLAF). We thank the MINOS Collaboration for use of its near detector data. We acknowledge the dedicated work of the Fermilab staff responsible for the operation and maintenance of the beamline and detector, and we thank the Fermilab Computing Division for support of data processing.

APPENDIX: PION KINEMATIC DISTRIBUTIONS

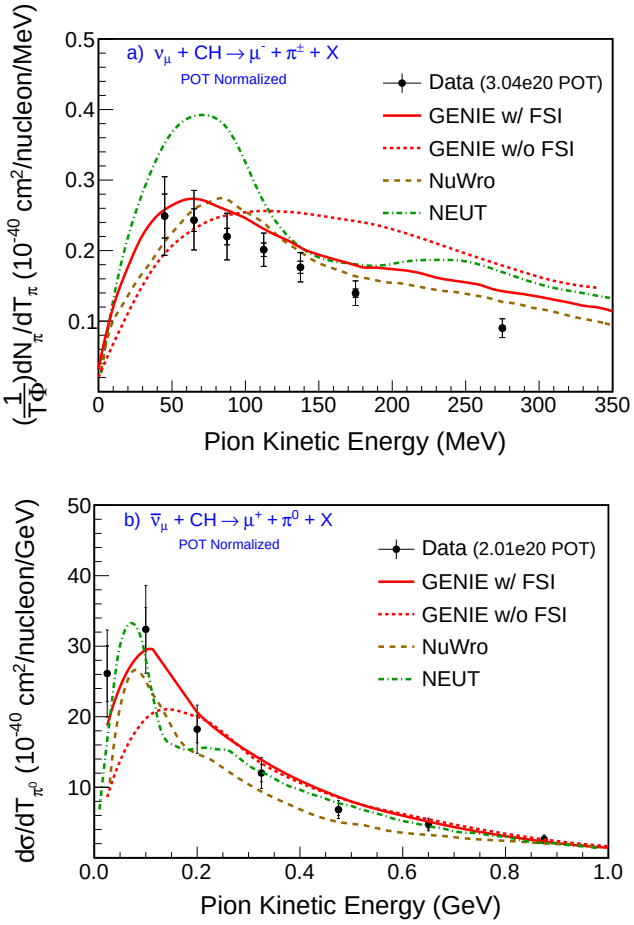

FIG. 15. Differential cross sections for pion kinetic energy, $d\sigma/dT_\pi$, for the ν_μ-CC(π^+) (a) and $\bar{\nu}_\mu$-CC(π^0) (b) samples. The data (solid circles) are compared to GENIE predictions neglecting versus including pion FSI (dashed vs solid-line histograms). Improved descriptions for shapes of the pion spectra are obtained with FSI effects included in the simulations.

Distributions for $\mu^\pm$ and related kinematic variables are featured by the main text. This Appendix presents distributions describing pion production kinematics for the two analysis samples. These figures represent updates to similar plots presented in the previous papers [5, 6], reflecting the improvements in the neutrino and antineutrino flux estimates noted in Sec. II A.

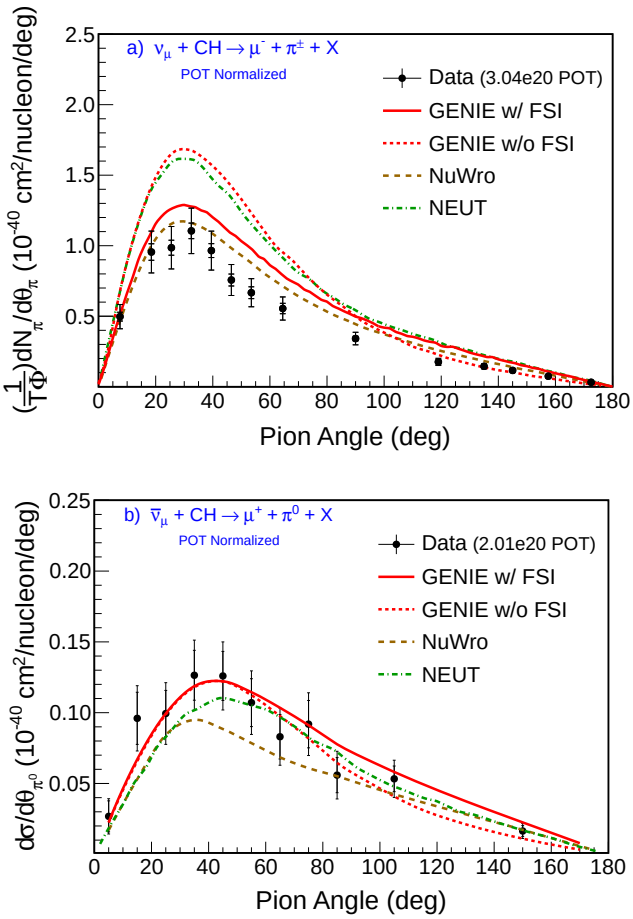

FIG. 16. Differential cross sections for the pion production angle with respect to the beam direction, $d\sigma/d\theta_\pi$, for the ν_μ-CC(π^+) (a) and $\bar{\nu}_\mu$-CC(π^0) (b) samples. As in Fig. 15, the data is compared to GENIE predictions without and with pion FSI effects included; marked improvement with the data is observed when pion FSI is taken into account (solid-line distributions).

Figure 15 shows the flux-averaged pion kinetic energy for the charged pions of the ν_μ-CC(π^+) sample (Fig. 15a), and for the π^0 of the $\bar{\nu}_\mu$-CC(π^0) sample (Fig. 15b). The kinetic energy ranges of π^+ and π^0 are different because the maximum π^+ energy is closely related to the detector depth. Figure 16 shows the polar-angle distributions for the produced $\pi^\pm$ and for the π^0 of these samples. The data points depict the same signal obtained with the same procedures reported in the main text, including the restriction on the invariant hadronic mass, $W < 1.8$ GeV. For the $\bar{\nu}_\mu$-CC(π^0) sample, the updated π^0 distributions are shown for the same energy

range, $1.5\,\mathrm{GeV} < E_\nu < 10\,\mathrm{GeV}$, as is used for the ν_μ-CC(π^+) sample. The quantity plotted for charged pions in Figs. 15a and 16a is same as in Ref. [5]. Events with one or more π^+ or π^- are included. Although not a true cross section, it arises from the cross section definition, Eq. (7), when each event can produce one or more pions. Each charged pion contributes one entry to a histogram and the cross section is calculated as in Sec. IV B.

Figures 15 and 16 show comparisons with GENIE, NEUT, and NuWro predictions; for both samples it is clearly seen that, for GENIE, the pion FSI treatment causes the simulation to move closer to the data. The main change in these updated results compared to the earlier ones is reduction of the large disagreement in absolute normalizations of the differential cross sections between data and GENIE-based predictions. This reduction comes about because the calculated data normalizations are now higher by 13% and 12% for the ν_μ and $\bar{\nu}_\mu$ event samples respectively as the result of revisions made to the flux estimates of the exposures as described in Sec. IV B. (Note that all pion distributions shown here are obtained using the $W < 1.8$ GeV selection; this cut was not applied in the π^0 distributions of Ref. [6].) Figures 15 and 16 show that the GENIE predictions are now closer to the data but still appear to be high, with the overall normalization difference exceeding 1σ in the ν_μ-CC(π^+) data set.

[1] K. Abe *et al.* (T2K Collaboration) Nucl. Instrum. Methods **659**, 106 (2011); arXiv:1106.1238.
[2] D.S. Ayres *et al.* (NOvA Collaboration), Report No. FERMILAB-DESIGN-2007-01, 2007.
[3] http://www.dunescience.org/.
[4] K. Abe *et al.* (Hyper-Kamiokande Proto-Collaboration) Prog. Theor. Exp. Phys. 053C02 (2015).
[5] B. Eberly *et al.* (MINERvA Collaboration), Phys. Rev. D **92**, 092008 (2015); arXiv:1406.6415.
[6] T. Le *et al.* (MINERvA Collaboration), Phys. Lett. B **749**, 130(2015); arXiv:1503.02107.
[7] U. Mosel, Phys. Rev. C **91**, 065501 (2015).
[8] C. Andreopoulos *et al.*, (GENIE Collaboration) Nucl. Instrum. Meth. Phys. Res., Sect. A, **614**, 87 (2010).
[9] Y. Hayato, Acta Phys. Pol. B **40**, 2477 (2009).
[10] T. Golan, C. Juszczak, and J.T. Sobczyk, Phys. Rev. C **86**, 015505 (2012).
[11] L. Aliaga *et al.* (MINERvA Collaboration) Nucl. Instrum. Methods Phys. Res., Sect. A, **743**, 130 (2013); arXiv:1305.5199.
[12] D. G. Michael *et al.* (MINOS Collaboration) Nucl. Instrum. Methods Phys. Res., Sect. A, **596**, 190 (2008).
[13] K. Anderson et al., FERMILAB-DESIGN-1998-01, (1998); P. Adamson *et al.*, arXiv:1507.06690.
[14] L. Aliaga *et al.* (MINERvA Collaboration) Nucl. Instrum. Methods Phys. Res., Sect. A **789**, 28 (2015); arXiv:1501.06431.
[15] S. Agostinelli *et al.*, Nucl. Instrum. Methods Phys. Res., Sect. A, **506**, 250 (2003).
[16] J. Allison *et al.*, IEEE Transactions on Nuclear Science, **53** No.1, 270 (2006).
[17] C. Alt *et al.* (NA49 Collaboration) Eur. Phys. J. C **49**, 897 (2007).
[18] D. S. Barton *et al.*, Phys. Rev. D **27**, 2580 (1983).
[19] A. V. Lebedev, Ph. D Thesis, Harvard University, 2007 [Report No. FERMILAB-THESIS-2007-76].
[20] J. Park *et al.* (MINERvA Collaboration), Phys. Rev. D **93**, 112007 (2016); arXiv:1512.07699.
[21] L. Aliaga *et al.* (MINERvA Collaboration) arXiv:1607.00704.
[22] A. Bodek and J. L. Ritchie, Phys. Rev. D **23**, 1070 (1981).
[23] D. Rein and L. M. Sehgal, Ann. Phys. **133**, 79 (1981).
[24] J. Beringer *et al.* (Particle Data Group), Phys. Rev. D **86**, 010001 (2012).
[25] K. S. Kuzmin, V. V. Lyubushkin, and V. A. Naumov, Acta Phys. Polon. B **37**, 2337 (2006); hep-ph/0606184.
[26] A. Bodek, I. Park, and U. Yang, Nucl. Phys. Proc. Suppl. **139** 113 (2005); hep-ph/0411202.
[27] S. A. Dytman and A.S. Meyer, AIP Conf. Proc. **1405** 213 (2011).
[28] D. Ashery *et al.*, Phys. Rev. C **23**, 2173 (1981).
[29] T.-S. H. Lee and R. P. Redwine, Ann. Rev. Nucl. Sci. **52**, 23 (2002).
[30] A. Higuera *et al.* (MINERvA Collaboration), Phys. Rev. Lett. **113**, 261802 (2014); arXiv:1409.3835.
[31] D. Rein and L. M. Seghal, Phys. Lett. B **657**, 207 (2007); arXiv:0606185.
[32] B. Eberly, University of Pittsburgh, PhD, 2014.
[33] D'Agostini, G., Nucl. Instrum. Methods Phys. Res., Sect. A, **362**, 487 (1995).
[34] L. Fields, J. Chvojka *et al.* (MINERvA Collaboration), Phys. Rev. Lett. **111**, 022501 (2013); arXiv:1305.2234.
[35] T. J. Bowles *et al.*, Phys. Rev. C **23**, 439 (1981).
[36] M. K. Jones *et al.* Phys. Rev. C **48**, 2800 (1993).
[37] Cross-section data points, their systematic uncertainties and correlations, plus the ν_μ and $\bar{\nu}_\mu$ fluxes of the exposures, are available as tables in the Supplement.
[38] S. L. Adler, Ann. Phys. (N.Y.) **50**, 189 (1968).
[39] S. L. Adler, Phys. Rev. D **12**, 2644 (1975).
[40] L. L. Salcedo, E. Oset, M. J. Vicente-Vacas, and C. Garcia-Recio, Nucl. Phys. **A484**, 557 (1988).
[41] G. M. Radecky *et al.* Phys. Rev. D **25**, 1161 (1982).
[42] T. Kitagaki *et al.* Phys. Rev. D **34**, 2554 (1986).
[43] C. Wilkinson, P. Rodrigues, S. Cartwright, L. Thompson, and K. McFarland, Phys. Rev. D **90**, 112017 (2014).
[44] H. J. Grabosch, *et al.*, Z. Phys. C **41**, 527 (1989).
[45] P. Rodrigues, C. Wilkinson and K. McFarland; arXiv:1601.01888.
[46] M. Martini, M. Ericson, G. Chanfray and J. Marteau, Phys. Rev. C **80**, 065501 (2009).
[47] J. Nieves, I. Ruiz Simo, and M. J. Vicente Vacas, Phys. Lett. B **721**, 90 (2013).
[48] C. Berger and L. M. Sehgal, Phys. Rev. D **79**, 053003 (2009).
[49] E. A. Paschos, J-Y. Yu, and M. Sakuda, Phys. Rev. D **69**, 014013 (2004).